Field experiment and FEM validation on fatigue performance of orthotropic steel decks composited with SFRC layer

Developments in the Built Environment 27 (2026) 100981

Contents lists available at ScienceDirect

Developments in the Built Environment

journal homepage: www.sciencedirect.com/journal/developments-in-the-built-environment

Field experiment and FEM validation on fatigue performance of orthotropic steel decks composited with SFRC layer

Rui-Xu Zhu [a], Zhi-Wen Zhu [a,*], Giuseppe Lacidogna [b,c]

[a] Department of Civil Engineering and Smart Cities, Shantou University, Shantou, 515063, China
[b] Department of Structural, Geotechnical and Building Engineering-DISEG, Politecnico di Torino, 24, Corso Duca Degli Abruzzi, Piedmont, Turin, 10129, Italy
[c] College of Architecture and Energy Engineering, Wenzhou University of Technology, 6th Floor, Administrative Building, South Campus, Wenzhou, 325000, China

ARTICLE INFO

Keywords:
Fatigue
Orthotropic steel decks (OSDs)
Steel fiber reinforced concrete (SFRC)
FEM
Random traffic flow

ABSTRACT

For small and medium-span bridges using the OSDs, compositing the steel deck with a SFRC layer may provide a cost-effective solution to fatigue induced by repetitively passing trucks. In this study, strain gauges were first instrumented on OSD during the construction of an actual bridge using this composite deck system. Then, two-week continuous stress monitoring under random traffic flows was conducted. The measured stress ranges at those fatigue-prone details are far below the CAFLs of their fatigue categories, implying high resistance against fatigue. To further validate the measured stress behavior, a three-dimensional FEM of the OSD-SFRC composite deck was then established and loaded by the AASHTO fatigue truck. The FEM results also show extremely low stress levels at those measured fatigue-prone details. The SFRC layer significantly enhances deck stiffness and suppresses local stress effects, and hence creates a fatigue-resistant deck system.

1. Introduction

Orthotropic steel deck (OSDs) has the advantages of light self-weight, large load-carrying capacity and a low life-cycle cost, hence it is a commonly employed structural system for long-span bridges. However, OSDs are characterized by complicated weld details, stress concentrations, and significant stress local effects under wheel loading. Meanwhile, welding can generate significant residual stresses at the welded details, making it prone to fatigue cracking under repetitive traffic loading (Connor et al., 2012). Fatigue cracking in OSDs can reduce the stiffness of the bridge deck, resulting in increased deflection of the pavement layer under overweight trucks. Additionally, the Young's modulus of traditional pavement using the stone mastic asphalt (SMA) or epoxy asphalt concrete decreases with the increase of temperature (Bocci et al., 2015), lowering its stiffness contribution to the deck system, which will increase OSDs deformation and stress level under wheel loads (Wu et al., 2013; Cui et al., 2018). Exposure to extreme weather and severe working condition further deteriorate the performance of deck overlay, which may lead to permanent deformation, cracking, debonding of the wearing course from the steel plate, formation of blisters and disintegration. That deterioration will seriously affect the normal traffic pattern on the bridge and may even threaten bridge safety. In recent years, the steel-UHPC (Ultra-high Performance Concrete) composite system has been widely used in OSDs (Ding and Shao, 2015; Pei et al., 2019). Shao and Cao (2018) conducted a fatigue assessment of a steel-UHPC lightweight composite deck using a multi-scale finite element method. The results indicated a notable decrease in stress at the fatigue-prone details of the orthotropic deck, and both the shear studs and the UHPC layer met the relevant fatigue requirements. Qin et al. (2022) conducted a study based on stress monitoring data from orthotropic decks under traditional asphalt concrete pavement and steel-UHPC pavement, demonstrating that the UHPC layer can effectively extend the fatigue life. This composite structural system can greatly reduce the high stress ranges at complicated weld details, such as rib-to-deck (RD), deck-to-floorbeam (DF). However, its fatigue improvement is limited for those details slightly away from the deck, such as rib-to-floor-beam (RF) and Cutout details, etc. (Zhu et al., 2016). It should be noted that besides its high costs, the construction of UHPC presents significant challenges for engineering application, such as steel fiber clumping, internal voids, and surface pitting on the UHPC layer. Improper curing may also lead to significant shrinkage, causing cracking in the UHPC layer (Su et al., 2021). In addition, the high cost prevents its application to small and medium-span bridges, where the required volume of UHPC is relatively

* Corresponding author.
E-mail address: zhuzw@stu.edu.cn (Z.-W. Zhu).

https://doi.org/10.1016/j.dibe.2026.100981
Received 28 April 2026; Received in revised form 15 June 2026; Accepted 23 June 2026
Available online 24 June 2026

small.

Steel fiber reinforced concrete (SFRC) is a typical composite material prepared by mixing randomly distributed short steel fibers into plain concrete. SFRC exhibits better performance on fatigue, impact resistance, crack control, and durability than plain concrete (Krstulovic-Opara et al., 1995). Therefore, recently SFRC has been widely used in buildings, road and bridge engineering (Zhang et al., 2020). Based on previous studies on steel-UHPC composite decks, it has been recognized that enhancing the stiffness of deck system is an effective solution to avoid fatigue cracking and overlay damage of the OSDs. Compared with commonly used UHPC layers in steel-UHPC composite decks, the SFRC layer in this study has a larger thickness and therefore increases the dead load of the bridge deck. The thicker SFRC layer is expected to improve the overall deck stiffness and hence the load-distribution capacity under truck loads, which may help reduce the stress at fatigue-prone OSD details. Therefore, the use of a 130 mm thick SFRC layer is considered a potential good solution for small- and medium-span bridges where fatigue improvement, low cost and construction feasibility are all required.

For small- and medium-span bridges, concrete decks are normally used since dead loads are not the major concerns due to not significant span length. However, when rapid construction is required, the OSDs may be used in steel girder, and the SFRC can be an option for its deck overlay. With this consideration, an OSDs composited with SFRC system has been developed and implemented (Ye et al., 2021). Such a system consists of a traditional OSDs system composited with a reinforced SFRC layer. The composite action between the two components is accomplished by shear studs. Since the mixture of SFRC includes coarse and fine aggregate, it creates good material mobility and is easy to mix evenly during manufacturing. Technically, the mixing process is much simpler than that of the UHPC. Hence, SFRC can be produced in most of commercial concrete mixing stations, and its material cost is only slightly higher than that of commercial plain concrete. In addition, SFRC does not require high-temperature curing and hence simplifies the construction process. Therefore, SFRC shows potential application in bridge engineering, especially in municipal small- and medium-sized bridges due to its cost-effective solution to OSDs bridge. However, the stress behavior and fatigue resistance of this bridge deck system, along with their inherent mechanisms, remain unclear. Comprehensive research is needed to provide an understanding for future engineering practice.

In this study, an in-service medium-span bridge using the OSDs composited with SFRC system was field tested and numerically analyzed to obtain the stress responses at fatigue-prone details of OSDs, as to study the structural behaviors and evaluate fatigue performance of the OSDs, which help demonstrate the feasibility of the fatigue-resistant OSDs composited with SFRC system in small- and medium-span bridges.

2. SFRC properties

Over the years, researchers (Meng et al., 2014, 2021; Picazo et al., 2021) have conducted performance enhancement on SFRC properties. It is widely recognized that short fibers in SFRC can delay the formation of cracks, while long fibers can bridge cracks, strengthen the tensile properties of concrete, and improve its ductility (Martinelli et al., 2015; Blasi and Leone, 2022). Comparative analyses reveal that fiber incorporation in plain concrete substantially improves multiple mechanical characteristics including but not limited to flexural strength, impact resistance, fatigue endurance, wear durability, deformation capacity, post-cracking load-bearing performance, and fracture toughness (Yang, 2012). The most important improvement by the addition of fibers to plain concrete is the increase in toughness and ductility (Yin et al., 1988). The stress redistribution created by steel fibers actively mitigates microcrack initiation and propagation induced by internal concrete stresses, which help transfer brittle fracture patterns into progressive ductile failure patterns (Caggiano et al., 2015).

The SFRC mixture used in this study is summarized in Table 1. The main materials for preparing the SFRC include PO 42.5R ordinary Portland Cement, granite stone with an apparent density of 2620 kg/m^3, fine sand with a density of 2660 kg/m^3 and an admixture. The admixture is a carboxylate-based high-efficiency water reducer with a concentration of 10.8%. The steel fiber is wave-shaped with a length of 38 mm, a width of 1.5 mm and a thickness of 0.8 mm, and its volume content is 55 kg/m^3. The tensile strength of steel fibers is 1100 MPa.

The C50 grade SFRC specimens for compression test and splitting tensile test were prepared in this study. The casting and finishing of SFRC specimens were made simultaneously with the pouring of SFRC layer on the bridge. The specimens were demolded approximately seven days after casting, and then cured at the natural environment in the laboratory (approximately 25°C temperature and 95% relative humidity) for 28 days before test. All tests were conducted according to the Codes (JG/T 472-2015, 2015; GB/T 50081-2019, 2019). The test results for the compressive strength, splitting tensile strength, its Young's modulus, and Poisson's ratio are presented in Table 2.

3. Bridge information and instrumentation

The bridge in this study serves traffic on a national highway, with a designed speed of 60 km/h. The bridge is a three-span continuous box-girder OSDs structure with span arrangement of (2×30)+(35 + 60+35)+(2×30) m, hence a medium-span bridge shown in Fig. 1a. The field monitoring was conducted on the northern span of 30 + 30 m, which accommodates a four-lane two-way traffic on the bridge deck. The main girder of this span features a steel single-box, double-cell cross section, with a girder height of 1.6 m at the bridge centerline and a standard width of 19.0 m, as shown in Fig. 1b. The OSDs in this bridge consists of a 16 mm thick deck plate, 8 mm thick trapezoidal-shaped ribs of 270 mm high spaced at a center-to-center distance of 600 mm, and solid floorbeams of a 14 mm web thickness at a spacing of 3 m. Fig. 1c shows the structural layout of the OSD. Shear studs with 60 mm height and 16 mm diameter are welded to the OSDs deck plate at spacing of 300 mm both in longitudinal and transverse direction. A double-layer, bidirectional reinforcement grid with 10 mm diameter bars spaced at 100 mm is then assembled, followed by the casting and curing of a 130 mm thick SFRC layer for at least 28 days. This forms an OSDs composited with SFRC system, as shown in Fig. 1c. In addition, 70 mm thick SMA overlay is applied on the top of the SFRC layer.

The sections near the bridge supports and the midspan are typically among the most critical sections for continuous beam bridges. In addition, easy access to the test section is also an important consideration for test convenience and personal safety. Hence, field monitoring positions were selected between pier 6 and abutment 7, as shown in Fig. 1a. In this study, the floorbeams were numbered from the expansion joint at northern end of the main girder adjacent to the southern approach, where the tested floorbeam was numbered as F4 and F12, as shown in Fig. 1a. Meanwhile, longitudinal ribs are numbered from the east side towards the central barrier. The trapezoidal-shaped ribs were numbered sequentially as U1 to U10. Based on the studies of fatigue crack formation in OSDs (Fu et al., 2017; Wang et al., 2020; Zhao et al., 2022), the fatigue-prone details considered in the field monitoring mainly include the rib-to-deck (RD) welds, rib-to-floorbeam (RF) welds, and the base metal at the floorbeam cutout (Cutout). The strain gauges at RD details located both at the deck plate side and rib wall side at the midway between adjacent floorbeams.

The strain gauges at RD weld detail were placed respectively between floorbeams F3 and F4 and between floorbeams F11 and F12.

Table 1
SFRC composition (Unit: kg/m^3).

Steel fiber	Cement	Sand	Stone	Water	Admixture
55	480	713	1032	155	9.6

Table 2
Properties of SFRC.

Concrete grade	Compressive strength/MPa	Splitting tensile strength/MPa	Young's modulus/GPa	Poisson's ratio
C50	64.8	4.2	39.0	0.16

Transverse position for stress monitoring was selected based on the design lanes on the bridge deck, specifically choosing the outmost lane commonly occupied by trucks. Therefore, the strain gauges are placed below the left wheel track on both sides of longitudinal ribs U1 and U2, as shown in Fig. 1b.

This study considers two other fatigue-prone details at the RF welding connection. The first is transverse stress (σ_{td}) on the floorbeam side at the low end of the RF weld (RF-F), with the stress direction normal to the weld toe line. The second is the vertical stress (σ_{vr}) on the rib wall at the lowest circumferential RF weld (RF-W), with the stress direction perpendicular to the weld toe at the bottom of the circumferential weld, i.e., along the RF weld direction on the mid-plane of the floorbeam (Zhang et al., 2017). The fatigue assessment in this study follows the nominal stress method outlined in the AASHTO specifications (AASHTO, 2017). The strain gauges at the floorbeam cutout were applied tangentially, with a 6 mm offset from the free edge. All other strain gauges are placed 6-mm from the weld toe and gauge axis along the stress direction, as shown in Fig. 2. Strain gauges of UFLA-2-11-3LT were used with a good self-temperature compensation capacity, and with a sensitive grid size of 2 × 3 mm. The placement of the strain gauges is shown in Fig. 2b–g.

4. Stress behavior under random traffic flows

After the bridge was opened to traffics for several months, the traffic flows were basically stable. Therefore, stress monitoring at various details of the OSDs under random traffic flows was conducted. Since the data-acquisition system used (DHDAS) could not provide a triggering mode to record the response under the passage of trucks, strain records were continuously recorded without filtering and transferred to stress records using the Young's modulus of 2.06×10^5 MPa of steel (Q345qC, which is a type of structural steel used for bridges in China with a yield strength of 345 MPa). Based on the designed traffic speed (60 km/h) and observed actual truck speeds, the sampling frequency of the data-acquisition system was set to 200 Hz. At 60 km/h, this provides approximately 4∼5 sampling points over the 390 mm longitudinal length (Zhu et al., 2018a,b), ensuring that complete stress records and details of the stress response are captured without missing true peak stresses. To account for potential differences in traffic patterns on weekdays and weekends, two weeks of continuous measurement of these details were carried out at the bridge site. Due to space limitations in this paper, only the measured results at the details beneath the left wheel trace of the tested lane were provided.

4.1. RD weld

For the RD weld details, strain gauges 6-5 and 6-6 are respectively applied to the deck plate side (RD-D) and rib wall side (RD-R). As shown in Fig. 3, the stress levels at the RD details under random traffic flow are very low, significantly below the constant range fatigue limit (CAFL) of the detail per AASHTO LRFD. The RD-D experiences alternative tensile and compressive stress, with an overall low stress level and the maximum stress range not exceeding 5 MPa. The RD-R stress is dominated by compression, with slightly higher stress range than the RD-D,

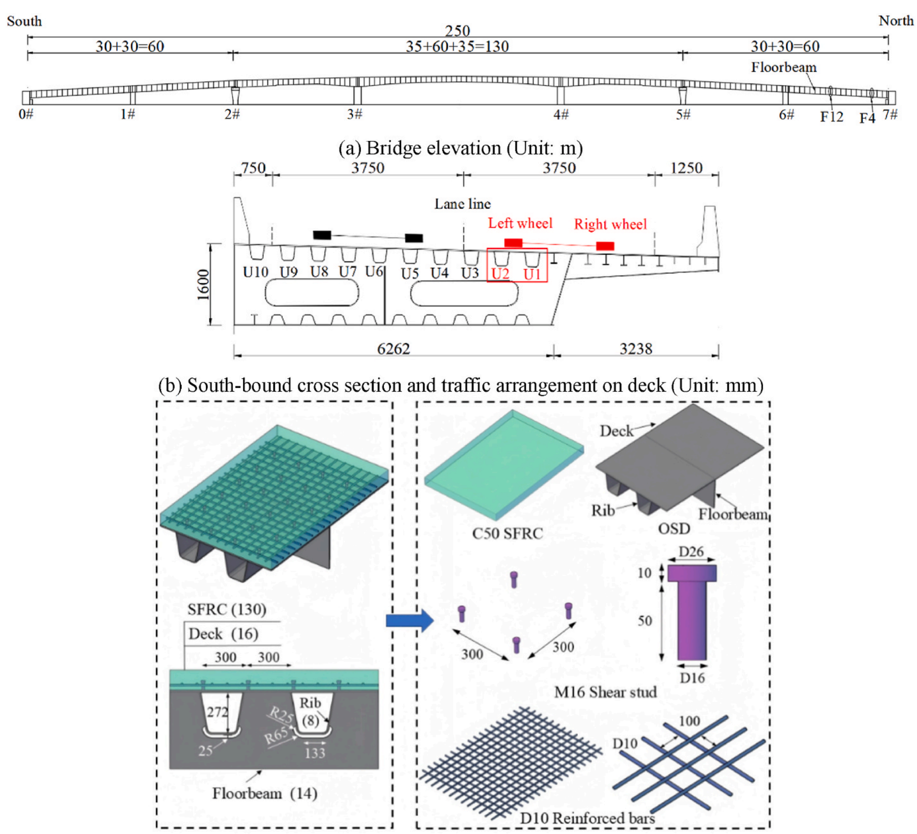

Fig. 1. Bridge layout and OSDs system.

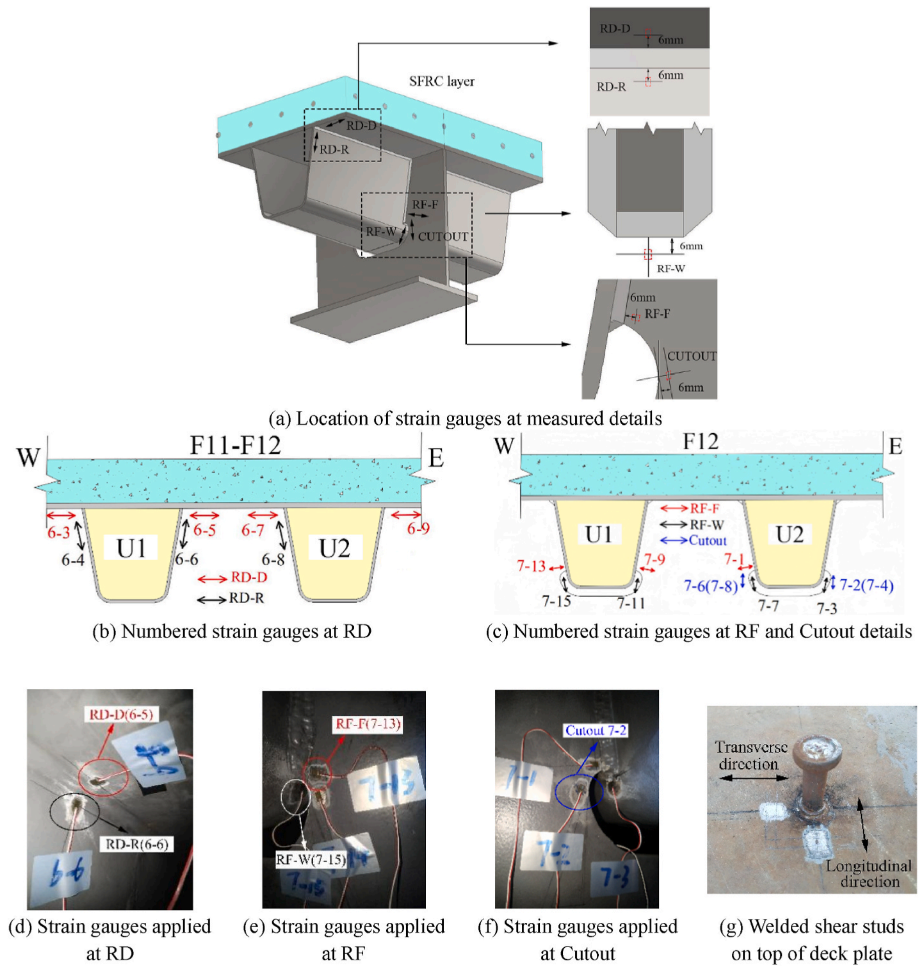

(a) Location of strain gauges at measured details

(b) Numbered strain gauges at RD

(c) Numbered strain gauges at RF and Cutout details

(d) Strain gauges applied at RD

(e) Strain gauges applied at RF

(f) Strain gauges applied at Cutout

(g) Welded shear studs on top of deck plate

Fig. 2. Strain gauge arrangements at details of OSDs and their installation photo on real bridge.

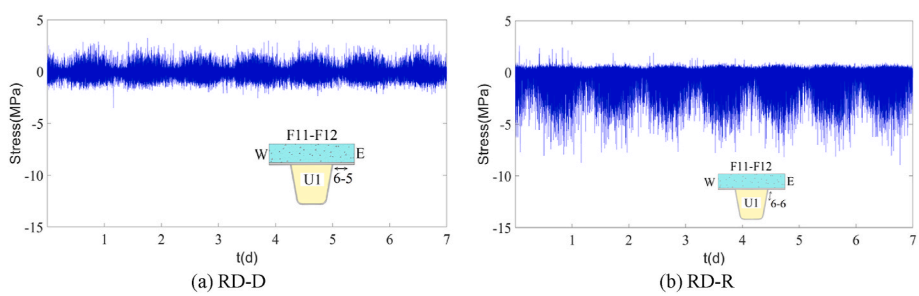

(a) RD-D

(b) RD-R

Fig. 3. 7d stress records at RD detail.

but the maximum stress range remains below 10 MPa. Compared to traditional pavement using SMA or epoxy asphalt concrete, the stress range at the deck plate side is typically greater than that at the rib wall side (Zhu et al., 2017a,b). This difference may be attributed to the large thickness of the SFRC layer, which enhances the deck stiffness of the deck plate. As a result, the load is distributed over a wider area on the deck plate, reducing the local stress effects produced by wheel loading. Consequently, the stress levels at the RD details, particularly at the RD-D, are significantly reduced.

In the following, the same truck passing the bridge deck at the same moment during the monitoring period was selected to compare the short-term stress responses generated at different weld details. Fig. 4 shows the typical stress responses of this truck at the RD details. The truck was identified as a five-axle truck, consisting of a front axle, a middle axle, and a tri-axle rear group. Each single axle generates a clearly individual stress cycle at both the deck plate side and the rib wall side at U1 and U2. Additionally, the short-term stress records of RD-D and RD-R differ a lot due to the global effect of the OSDs' system in transverse direction (Connor et al., 2012; Li et al., 2024). Before the wheel load directly acts at the RD detail, the wheel load is transmitted to the deck plate at the RD detail through longitudinal ribs. This transverse global effect causes bending at the deck plate side, generating tensile stress at RD-D. The superposition of the global and local effect changes the stress from tension to compression, and the closer the detail is to the wheel load in transverse direction, the greater the stress ranges will be created. Due to the large thickness and stiffness of the SFRC layer, the rib wall beneath the wheel load behaves like a compression column supporting the deck plate, hence generating significant compressive stress.

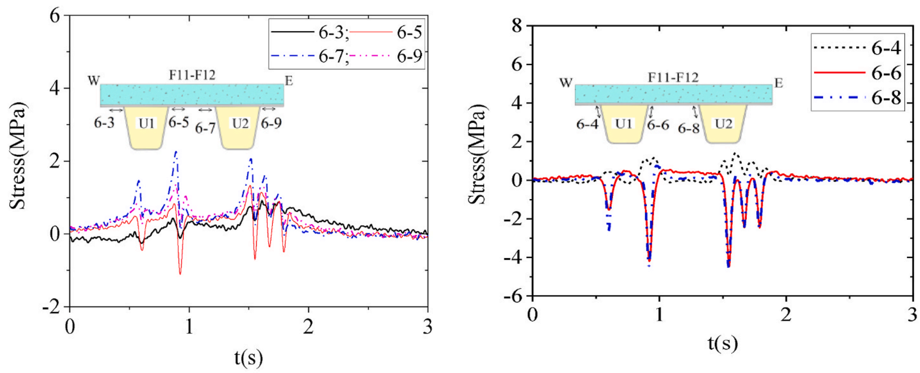

(a) RD-D (b) RD-R

Fig. 4. Typical stress records at RD detail under truck loading.

4.2. RF weld

Fig. 5a–b presents the 7d stress records at the RF-F and RF-W details. The stress level at RF-F (7-13) is extremely low, while RF-W (7-15) exhibits a slightly increased tensile-compressive stress. However, the stress levels at both RF-R and RF-W details are significantly lower than their respective CAFL.

Considering the short-term stress response at the two RF details, when the five-axle truck loaded at the details at the same instant as that shown in Fig. 6, the RF detail exhibits stress characteristics similar to those observed in OSDs with SMA overlay or with steel-UHPC composite deck (Zhang et al., 2020; Gao et al., 2025). At the RF details, individual axles within the axle group cannot be clearly distinguished. Due to the wheel offsets to U1 and U2, longitudinal ribs experience sectional torsion under wheel loading, resulting in distortion at the RF-W detail, resulting in tensile or compressive stress at the RF-W, which is highly dependent on its location to the wheel loads. For U1, the left side is under compression and the right side is under tension, whereas U2 exhibits the opposite behavior. Based on the stress levels at the RF-F and RF-W details, the wheel is laterally loaded between U1 and U2, and is closer to U1.

At the left side of U1, strain gauge 7-15 records the maximum stress response, with a tensile stress peak value of 14.1 MPa, while strain gauge 7-11 is primarily under compression, with a compressive peak stress of 5.2 MPa. It is evident that each axle generates a stress peak, but these peaks are no longer independent. Instead, they form peaks on a higher stress platform, presenting a "camelback" effect. This phenomenon is particularly clear under the rear triplex axle.

4.3. Cutout detail

The Cutout detail is characterized as the highest fatigue category of A in OSD, with a CAFL of 169 MPa. Due to severe stress concentration and the combined in-plane and out-of-plane stresses presented on the Cutout (Ding and Shao, 2015), the stress level under wheel load is notably higher than other details in OSDs. Hence this detail is also prone to fatigue cracking under repetitive truck loading (Chen et al., 2021; Li et al., 2021). In this study, 7d stress records were obtained from strain gauges located on both the north and south sides of the floorbeams F4 (near the support) and F12 (at midspan), as shown in Fig. 7. Strain gauges 4-2 and 7-2 were placed on the north side of the floorbeam facing the traffic flow, while strain gauges 4-7 and 7-4 were placed on south side. The stress levels at the north side are higher than those at the south side. Additionally, although the stress levels at the inner edge of the cutout are significantly higher than those at the RD and RF details, they are still much lower than the CAFL of this detail. Both the north and south sides of the Cutout are subjected to combined tensile and compressive stresses, but compressive stress dominates significantly (Zhang et al., 2016). However, there are considerable differences in stress ranges among the four locations. The maximum compressive stresses at support floorbeam F4 and midspan floorbeam F12 are 20 MPa and 25 MPa, respectively, with the midspan floorbeam experiencing higher stress levels than the support floorbeam.

The short-term stress response at Cutout details under the same five-axle truck are shown in Fig. 8. The stress curves at different cutout locations are very similar, with compressive stresses higher than tensile stresses, but the stress responses on both sides of the same longitudinal rib are not identical. The passage of this five-axle truck generates three stress peaks at the details, implying that the rear tri-axle group produces only one single stress peak, and the stress curves cannot distinguish individual axles among the tri-axle group. At floorbeam F4, the compressive peak stress ranges at strain gauges 4-1, 4-2, and 4-7 are 4.4 MPa, 2.9 MPa, and 5.3 MPa, respectively. At floorbeam F12, the compressive stress peak ranges at strain gauges 7-2, 7-4, 7-6, and 7-8 are 3.0 MPa, 5.1 MPa, 8.1 MPa, and 8.0 MPa, respectively.

After obtaining the stresses at the same Cutout detail on its north and south sides of the floorbeam web, the in-plane and out-of-plane stresses, σ_{in} and σ_{out} at the Cutout detail can be obtained using the following

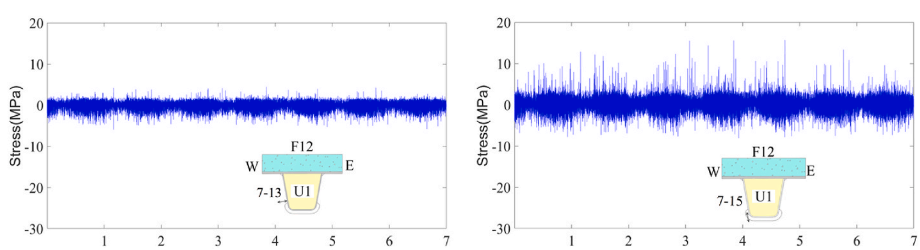

(a) RF-F (b) RF-W

Fig. 5. 7d stress records at RF detail.

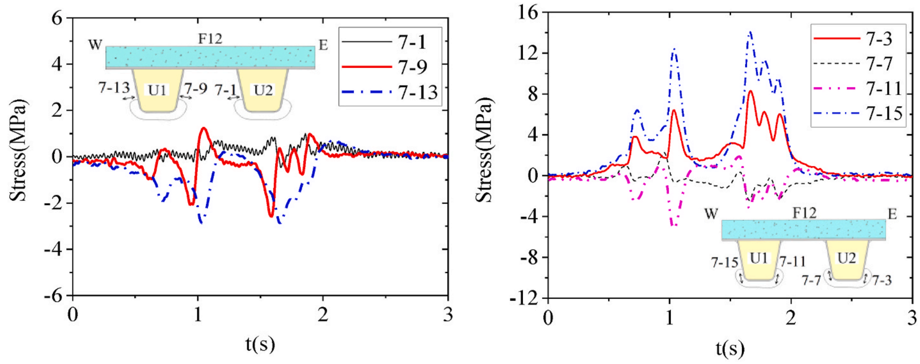

Fig. 6. Typical stress records at RF detail under truck loading.

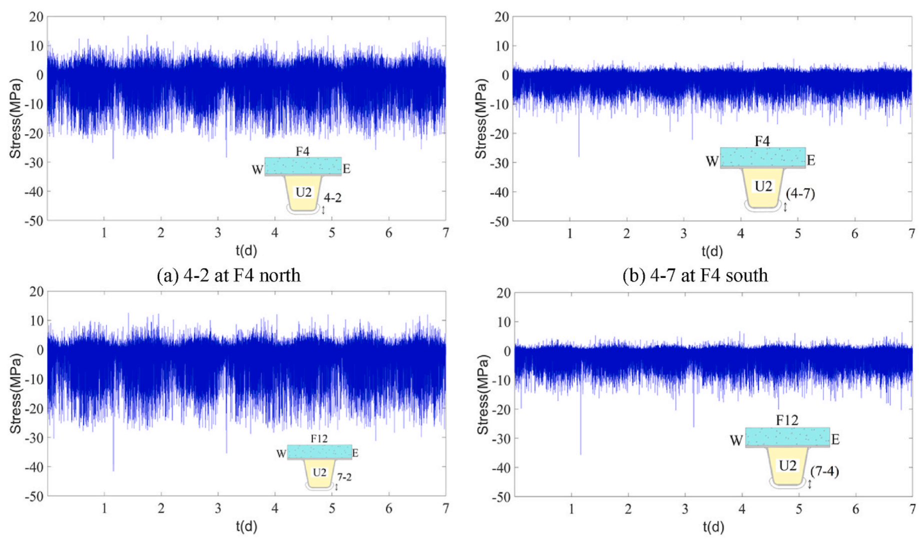

Fig. 7. 7d stress records at cutout detail.

equations (Xiang and Zhu, 2021; Fang et al., 2023):

$$\sigma_{\text{in}} = (\sigma_N + \sigma_S)\,/\,2, \sigma_{\text{out}} = (\sigma_N - \sigma_S)\,/\,2 \tag{1}$$

σ_N and σ_S are the stresses measured on the north and south sides of the floorbeam Cutout detail, respectively.

Under wheel loading, the floorbeams act as supports to longitudinal ribs. This is why the Cutout detail is always dominated by compressive stress. While from Fig. 8c–d, the response of strain gauges 7-2 on the north side of the floorbeam is slightly higher than that of strain gauges 7-4 on its south side, indicating that the floorbeams undergoes a certain degree of out-of-plane deformation under wheel loading. This is due to the rotation of longitudinal ribs under wheel loading, which is connected to the floorbeams and drives the floorbeam to experience the out-of-plane bending deformation. From the comparison of in-plane and out-of-plane stress components in Table 3, the Cutout detail is clearly dominated by in-plane stress. At floorbeam F4, the in-plane compressive stress reaches −28.5 MPa, accounting for approximately 98% of the total stress at Cutout detail. At floorbeam F12, the in-plane stress reaches −38.7 MPa, accounting for about 93% of the stress at Cutout detail. This indicates that, although the composite deck significantly increases the stiffness of the deck system, out-of-plane deformation of the OSDs floorbeam still occurs, although it is not significant compared to traditional epoxy asphalt paved OSDs.

5. FEA model, results and discussion

5.1. FEA model

To analyze the deformation characteristics and mechanical mechanisms at OSDs fatigue-prone details under wheel loading, this paper establishes a finite element model of the OSDs composited with SFRC system using ANSYS software. This model is built to simulate the stress response of various details under the passage of the truck's wheel in driving direction. The model is based on the construction drawings of the actual bridge and consists of the bridge deck plate, floorbeams 1 and 2, three spans of longitudinal ribs U1 to U4, shear studs, and the SFRC layer. The welds and dimensions of the OSDs details were explicitly modeled and the Young's modulus of the SFRC was set to 3.90×10^4 MPa based on the test result in Table 2, and that of the steel was set to 2.06×10^5 MPa.

Since the fatigue analysis in this study is based on the nominal stress method and the corresponding fatigue rating categories specified in the AASHTO LRFD, the fatigue loading was applied using the fatigue truck model HS-15 from this code for the OSD. The tire contact area is 510 mm (transverse) × 250 mm (longitudinal). The stiffness contribution of the 70 mm thick SMA overlay on the SFRC is ignored, while only to consider its load distribution effect. The wheel load is assumed to spread at a 45 angle to the top surface of the SFRC, resulting in a contact area of

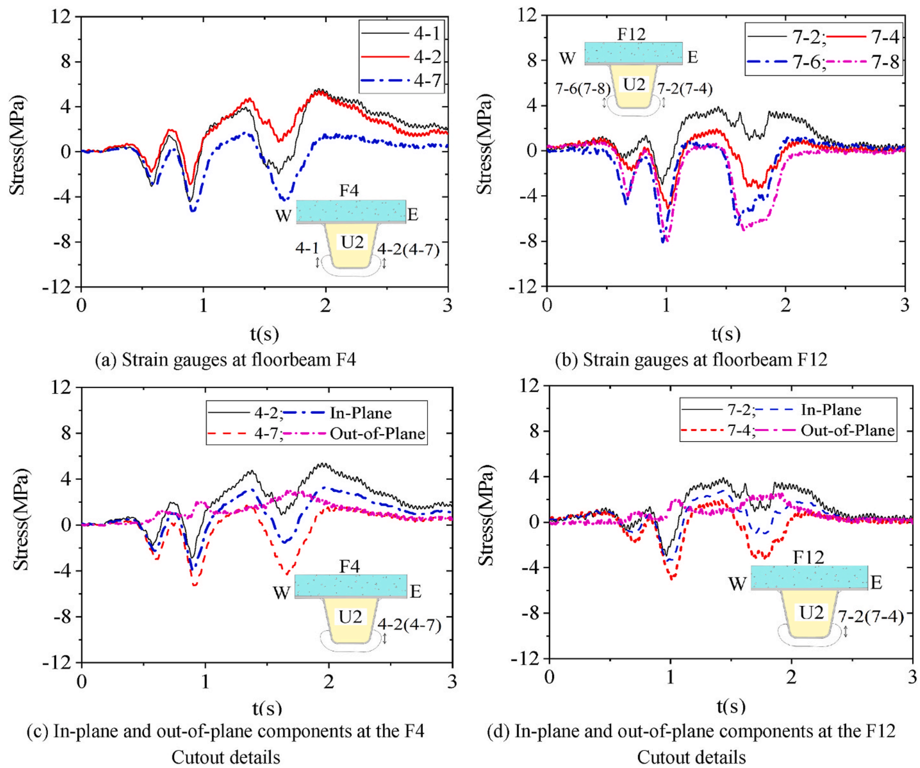

(a) Strain gauges at floorbeam F4
(b) Strain gauges at floorbeam F12
(c) In-plane and out-of-plane components at the F4 Cutout details
(d) In-plane and out-of-plane components at the F12 Cutout details

Fig. 8. Typical stress records at Cutout details under truck loading.

Table 3
Maximum stress ranges among 7d at Cutout detail (Unit: MPa).

Location	Point	Stress range	In-plane stress	Out-of-plane stress	Out/All
F4 north	4-2	−28.9	−28.5	−0.4	98%
F4 south	4-7	−28.1			
F12 north	7-2	−41.6	−38.7	−3.0	93%
F12 south	7-4	−35.7			

650 mm (transverse) × 390 mm (longitudinal). Since the spacing between adjacent floor beams on this bridge is only 3.0 m, which is significantly shorter than the spacing between the steering and middle axle group, let alone the spacing between the middle and rear axle groups. In this study, only one out of the rear-axle group is selected and applied as wheel loads to the OSDs, i.e., the tandem axle group with 1.2 m spacing between the two individual axles and the weight of a single wheel is 108/4 = 27 kN (Fu et al., 2019; Zhu et al., 2022).

A coordinate system is defined, with the origin at the intersection of the U1 symmetrical plane and the mid plane of floorbeam 2 on the deck plate. The X-axis is aligned with transverse direction, while the Y-axis is vertical, and the Z-axis is along the bridge longitudinal direction. Longitudinal position Z is defined as the distance from the front axle inside the tandem axle to the coordinate origin, and is directed to the south of the model. Due to limited space in this paper, only the most critical loading location in bridge transverse direction, i.e., the riding-rib-wall loading case to the OSDs is considered (Xiao et al., 2008; Wang et al., 2020; Zhu et al., 2023), specifically, the wheel centered on the east web of U3 (X = 1.05). Under this transverse loading location, longitudinal loading of the fatigue vehicle is simulated by moving the tandem axle in the positive Z-direction. The wheel load is moved in uniform step size of 0.1 m, starting from the midway of the north-side longitudinal rib at floorbeam 1 (Z = −4.5 m) and ending when the rear axle of the tandem reaches the midway of the south-side longitudinal rib at floorbeam 2 (Z = 1.5 m). Thus, longitudinal loading length is 6 m, corresponding to

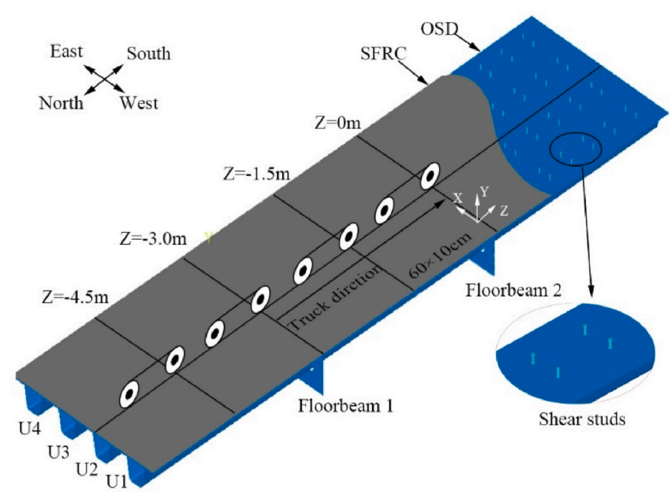

Fig. 9. FEA model and loading scheme.

60 load steps, as shown in Fig. 9.

The OSDs structure, shear studs, and SFRC layer are modeled using the three-dimensional solid element SOLID45, which is an 8-node element, with 3 translational degrees of freedom at each node. The shear studs are explicitly meshed, with their bottoms sharing nodes with the deck plate and their sides and tops sharing nodes with the surrounding SFRC. In the analysis, it is assumed that no tensile debonding occurs between the SFRC layer and the deck due to measured low stress under truck passage. This is implemented by coupling only the vertical displacements of the nodes at those interfaces between the studs and the SFRC layer, while displacements in other directions are allowed, such as the horizontal slip, as this treatment has a negligible influence on the stress at fatigue-prone details (Zhu et al., 2019). The model and grid arrangement are shown in Fig. 10.

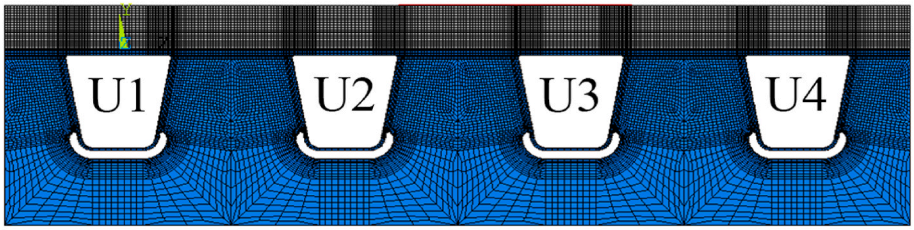

(a) Mesh arrangement of FEA model

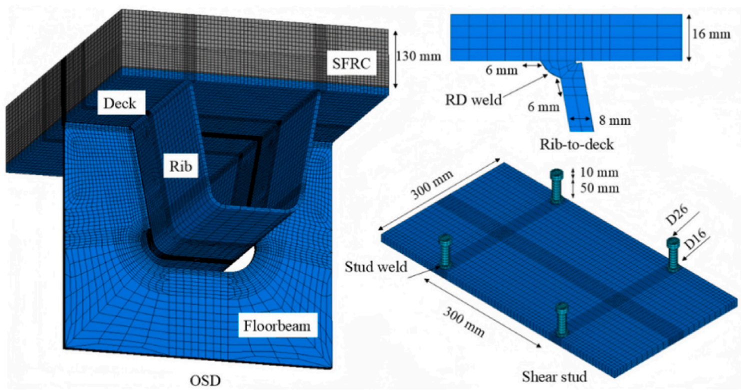

(b) OSDs mesh

Fig. 10. Finite element model and mesh arrangement.

In the model, the bottom of the floorbeams and the edges of the deck are fully fixed. Only the longitudinal displacement is constrained along the bridge direction. Since solid elements are used, it is necessary to control the mesh quality and quantity of the model to ensure computational feasibility and accuracy. Additionally, a controlled mapping method was employed for mesh generation. Therefore, sufficiently refined mesh in the region of interest is arranged to capture high stress gradient in the vicinity of a stress-concentrated area, while coarse elements were employed elsewhere to balance the computational efficiency and accuracy. The total number of elements is approximately 680,0000, with about 760,0000 nodes. The minimum size of the elements is 3 mm.

5.2. FEA results and discussion

Considering the transverse mechanical characteristics of the OSD, the riding-rib-wall loading case represents the most unfavorable transverse case for the OSDs (Zhu et al., 2023). The FEA obtains the stress responses at the RD, RF and Cutout details. Additionally, 3D stress contour plots and deformation patterns at critical locations are generated.

1) RD Details

The FEA obtained the stress response curves at the RD details on the left side of U3 at three longitudinal positions between floorbeam 1 and 2: Z = −0.37 m (L/8), −0.75 m (L/4), and −1.5 m (L/2), as shown in Fig. 11. The L/2 position exhibits the highest stress range, confirming the rationality of longitudinal placement of the instrumented RD details. Additionally, the consistently low stress responses observed across all three longitudinal positions suggest that wheel-load-induced stresses at the RD detail demonstrate stronger global stress effect than local stress effect. As the location of the RD-D detail approaches the floorbeam, the tensile peak stress range gradually decreases to 50%. This is because the stiffness of the OSDs' system increases near the floorbeam, leading to a reduction in the overall stress level. In contrast, the compressive stress dominates at the RD-R side, and each axle still generates clearly individual stress cycle, which is consistent with the measured results. The enhanced load distribution capacity of the thickened SFRC layer manifests as spatially extended stress peaks across the deck plate.

Comparing the FEA results with the measured results, at the RD-D side, the simulated stress range is 1.8 MPa, while the measured

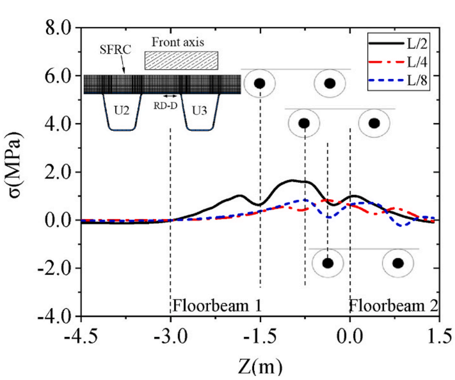

(a) RD-D

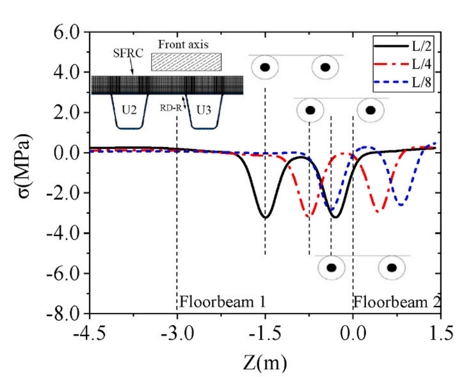

(b) RD-R

Fig. 11. Stress at RD detail with respect to wheel location.

equivalent stress range is approximately 5.0 MPa, indicating that the FEA result is lower. At the RD-R side, the finite element value is 3.6 MPa, also lower than the measured value. In the finite element model, the stress range at the RD-R detail is slightly higher than at RD-D, meaning RD-R is the more critical detail, which is consistent with the measured trend. It is noteworthy that although both the measurements and the finite element analysis show that the stress level at the RD details of the composite deck is within the same relatively low range (neither exceeding 5 MPa), the FEA results remain systematically slightly lower than the measured values. Referring to the rear tandem axle of Fatigue Vehicle Model III specified in the code (JTG D64-2015, 2015), the single-wheel load is 240/4 = 60 kN. This suggests that the HS-15 fatigue vehicle model used may underestimate actual fatigue loading effects under random traffic flows on the bridge deck in the studied region, implying that the axle weight of the AASHTO LRFD fatigue vehicle model is relatively conservative.

At Z = −1.5m (The front wheel center is located the midway between floorbeams 1 and 2), the partial von Mises stress distribution from the FEA is shown in Fig. 12. Fig. 12a illustrates the cross-section view at Z = −1.5 m, and Fig. 12b shows longitudinal section within the range of L/8 to 7L/8 between floorbeams 1 and 2. The analysis demonstrates three dominant deformation patterns: transverse deck plate deflection, longitudinal rib deformation, and rib wall warping. Since the riding-rib-wall wheel load centered directly above the RD detail of the U3, the local stress effect generates support negative moments M_1 and M_2. This induces bending stress and deformation at the deck plate side. At the same time, due to the overall transverse bending effect at the deck plate, tensile stress is generated at RD-D inner and outer sides. The stress gradually decreases outward from the RD detail under wheel loading. Longitudinal ribs are not only subjected to longitudinal bending but also experience warping stress and deformation caused by torsion, as well as compressive stress induced by the wheel load. Maximum compressive stresses on longitudinal rib wall surfaces occur at the load centerline, with inner and outer web sides primarily sustaining compressive stresses.

The wheel-load-induced deflection-to-span ratio (d/L) of the OSDs deck plate should not exceed 1/700 (JTG D64-2015, 2015), as shown in Fig. 13. The FEA results indicate that the absolute deflection of the deck plate at floorbeams d_1 and d_2 are 0.0469 mm and 0.0438 mm in transverse direction, respectively. The absolute deflections at the RD details are 0.0406 mm, 0.0470 mm, and 0.0342 mm, while the relative deflection values at d_1 and d_2 are both 0.0032 mm, i.e., a deflection-to-span ratio of only 1/100,000 at the deck plate. In longitudinal direction, under a span of 3 m between the diaphragm, the deflection d of the deck plate is 0.042 mm, corresponding to a deflection-to-span ratio of 1/71, 429. These deflection-to-span ratio are two orders of magnitude below code limits, confirming that the composite deck system have sufficiently high flexural rigidity.

2) RF details

Fig. 12b shows the von Mises stress contour of the RF detail, and Fig. 14 presents its stress response curve. It can be observed that compressive stress dominates at the RF-F detail, with a peak compressive stress of 2.9 MPa, while tensile stress clearly dominates at RF-W, with a peak tensile stress of 8.2 MPa. This indicates that within the composite structure, RF-W is the most critically stressed location among the RF details, a conclusion consistent with the measured results. Field measurement data show that the equivalent stress range at RF-F is approximately 5.4 MPa, and at RF-W it is about 8.8 MPa. Similarly, the stress ranges obtained from the FEA are within the same relatively low range as the measured values, they remain slightly lower than the measured value.

3) Cutout details

The stress curves at Cutout details are shown in Fig. 15a. The peak stress range at Cutout 1 and Cutout 2 are 13.9 MPa and 10.4 MPa, respectively. This demonstrates marginally lower stress ranges compared to experimental measurements with compressive stress dominance. The obtained stress curves cannot identify individual single axle, which is consistent with the measured stress characteristics.

When Z = −3.0m (where the front wheel center is at floorbeam 1), the deformation and von Mises stress contour of floorbeam 1 are shown in Fig. 15b. The results indicate that the maximum vertical deformation occurs beneath the wheel load center, with deformation gradually decreasing toward both sides of the wheel load. The Cutout details exhibit clear compressive deformation. Additionally, since the rear wheel load center acts on the north span of floorbeam 1, the floorbeam experiences out-of-plane bending deformation.

In terms of stress range, the FEA results and the measured results both fall within a similarly low stress range: the stress ranges at the RD details do not exceed 5 MPa; the RF-W detail ranges between 5 and 10 MPa; similarly, the Cutout detail exhibits the highest stress level in both the simulation and measurements, with stress ranging from 10 to 20 MPa. Regarding stress characteristics, the RD details generate distinct stress peaks under wheel loading, while the RF and Cutout details show only one prominent main stress peak. Not all measurement points can capture the complete peak corresponding to each axle load, which aligns with the measured results. Therefore, based on the consistency in stress levels and response characteristics, the finite element calculation results can be considered reliable.

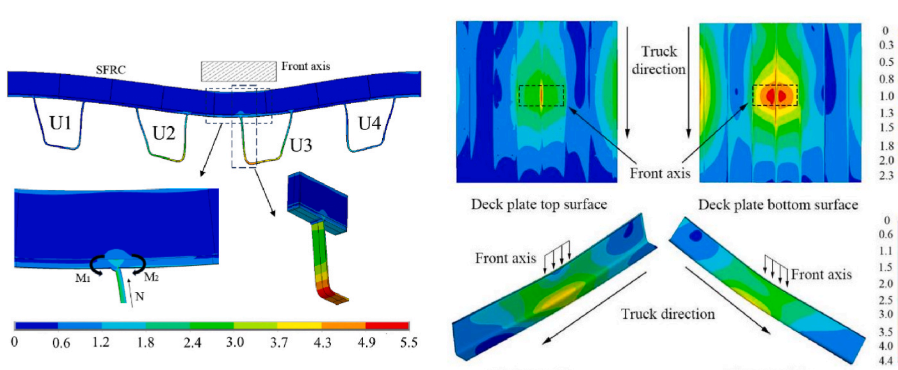

(a) Local deformation and stress

(b) Rib and deck plate deformation and stress

Fig. 12. Stress contour plot and deformation under wheel loading (Unit: MPa).

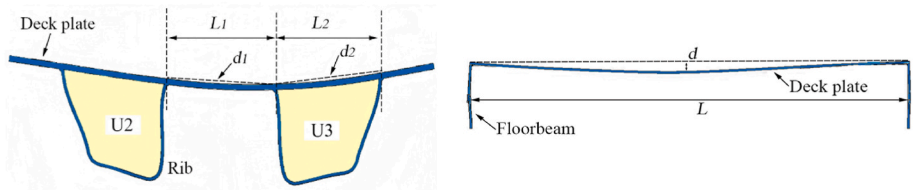

(a) Transverse direction (b) Longitudinal direction

Fig. 13. Schematic plot of deflection-to-span ratio of deck plate.

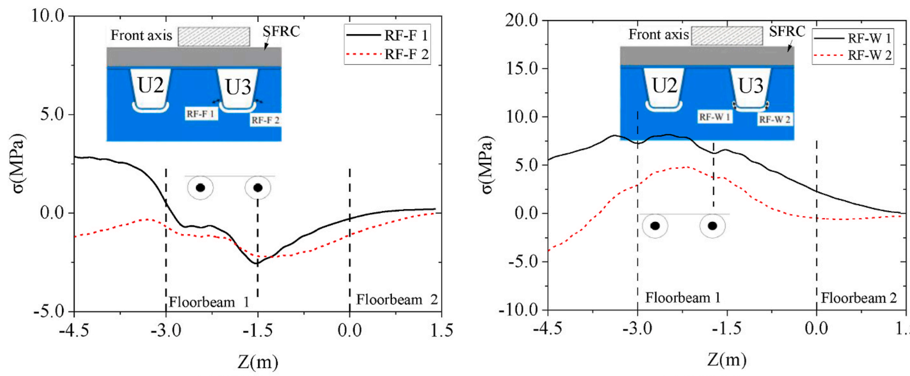

(a) RF-F (b) RF-W

Fig. 14. Stress at RF detail with respect to wheel location.

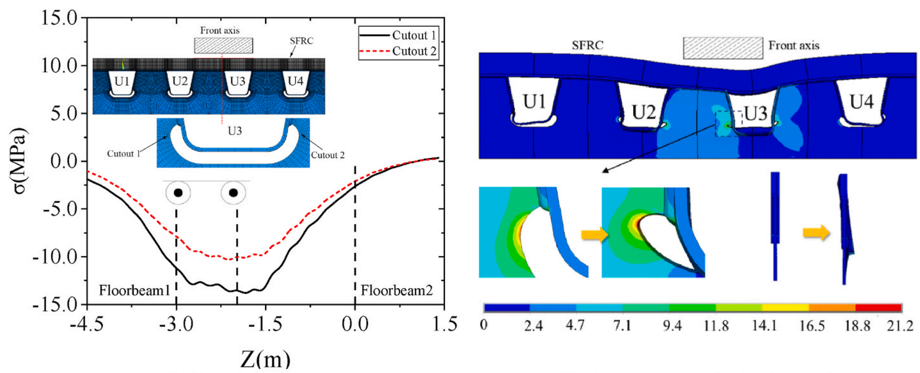

(a) Stress curve (b) Stress contour plot (Unit: MPa)

Fig. 15. Stress curve and contour plot at Cutout with respect to wheel location.

6. Stress spectrum and fatigue life of OSD

6.1. Stress spectrum

Based on the rainflow counting method, the stress-range spectrum at the details under the random traffic flows condition can be obtained. According to the Miner's rule, the variable-amplitude stress-range spectrums could be represented by the equivalent constant-amplitude stress ranges or effective stress ranges $S_{r,eff}$ using equation (2):

$$S_{r,eff} = \left(\sum \frac{n_i S_i^m}{\sum n_i} \right)^{1/m} \tag{2}$$

where n_i is the number of loading cycles at the stress range of S_i; m is the slope of the fatigue S-N curve of the detail, which is taken as 3 according to the AASHTO LRFD.

It is commonly recognized that small cars and light trucks, due to their light axle loads, do not cause significant fatigue damage to the OSDs details. Therefore, their loading effects can be ignored in the fatigue damage assessment at the details (Tong et al., 1997). Considering the measured stress level at this detail, the stress ranges below 4 MPa are not considered when calculating the equivalent stress range for category C details. Similarly, for the Cutout details with a fatigue category of A, the stress ranges below 12 MPa will also not be considered.

Table 4 presents the equivalent stress ranges, maximum stress ranges, and average daily loading cycles for the RD details during the monitoring period. The equivalent stress ranges for RD-D and RD-R are close, at 5 MPa and 5.5 MPa, respectively. The maximum stress ranges observed for RD-R is 12.0 MPa. Additionally, the average daily loading cycles for RD-D are generally much lower than that of RD-R, as the composite system significantly increases the stiffness of the deck plate, greatly reducing the stress on the deck plate side under wheel loading.

For the RF details. Its equivalent stress range is approximately 5.4 MPa. Clearly, the equivalent stress range at RF-W detail is high, with a maximum value of 8.8 MPa. The maximum stress range observed for RF-W is 39.6 MPa, approximately four times higher than that of RF-F. The highest average daily loading cycles for RF-F is 110.0, which is

Table 4
Stress ranges at fatigue-prone detail.

Details	Point	S_{max} (MPa)	$S_{r,eff}$ (MPa)	$\bar{n}$ (times/day)
RD-D	6-3	5.0	5.0	0.5
	6-5	6.7	5.1	6.0
	6-7	6.9	5.0	18.0
	6-9	5.8	5.0	15.5
RD-R	6-4	10.9	5.5	52.0
	6-6	11.5	5.4	337.5
	6-8	12.0	5.5	466.5
RF-F	7-1	8.5	5.3	21.5
	7-9	10.3	5.4	68.0
	7-13	10.4	5.4	110.0
RF-W	7-7	27.0	7.9	1147.0
	7-11	39.6	8.8	1827.5
	7-15	23.7	6.3	785.5
Cutout	4-2	42.4	18.2	536.0
	4-7	33.6	14.7	64.0
	7-2	54.0	19.7	603.5
	7-4	42.5	15.2	92.5

much lower than RF-W of 1827.5. Since both details have a fatigue category of C, it can be concluded that, at the RF weld, RF-W is more critical than RF-F in terms of fatigue.

The equivalent stress ranges at each strain gauges do not show significantly different, but those on the north side facing the traffic flow are slightly greater than those on the south side. Consequently, the average daily loading cycles on the north side is also higher. The maximum stress range at the midspan floorbeam F12 is 54.0 MPa, which is slightly greater than that at floorbeam F4.

6.2. Fatigue life evaluation

Fatigue evaluation was conducted based on nominal stress methos, as specified in AASHTO LRFD, the maximum stress ranges at the RD and RF details are significantly lower than the constant amplitude fatigue limit (CAFL) of fatigue category C (CAFL = 69 MPa), while the maximum stress range at the Cutout details is also notably lower than the CAFL of fatigue category A (CAFL = 165 MPa). Therefore, the fatigue life at all OSDs details can be considered infinite per AASHTO LRFD, as Y_1 shown in Table 5.

This paper attempts to estimate the fatigue life of OSD are also carried out based on fatigue damage using the codes. (JTG D64-2015, 2015; EN 1993-1-9:2005, 2005) i.e.,

$$\Delta\sigma_R^m N_R = \Delta\sigma_c^m \times 2 \times 10^6 \tag{3}$$

where $\Delta\sigma_R$ and N_R are the given stress range and the corresponding number of loading cycles related to a constant stress range; $\Delta\sigma_c$ is the fatigue strength under a given number of cycles of 2×10^6 under constant amplitude fatigue loading for the detail. In addition, the fatigue categories for RD and RF are FAT71, and for the Cutout detail is FAT100 (Zhu et al., 2018a,b). Their cutoff stress ranges are 26.2 MPa and 36.9 MPa, respectively.

The fatigue damage caused by n_i loading cycles under the stress range $\Delta\sigma_R$ is calculated using Equation (4), With the measured stress spectra, the cumulative damage degree D at the detail can be obtained, and the corresponding fatigue life Y_2 (Lim et al., 2014; Zhu et al., 2017a, b) can be calculated using equation (5):

$$D = \sum_i^n \frac{n_i}{N_R} = \sum_i^n \frac{n_i}{2 \times 10^6}\left(\frac{\Delta\sigma_c}{\Delta\sigma_R}\right)^m \tag{4}$$

$$Y_2 = 1 / (365D) \tag{5}$$

Fatigue life Y_2 based on fatigue damage are shown in Table 5. Their fatigued life at each OSDs detail is extremely higher than the 100-year of design life of the bridge. Therefore, like the obtained fatigue life based on AASHTO LRFD, it can be concluded that all OSD details have sufficient resistance against fatigue.

Table 5
Fatigue life of various details.

Details	Points	S_{max} (MPa)	Y_1(year)	D	Y_2(year)
RD-D	6-5	6.7	infinite	0	infinite
RD-R	6-6	11.5	infinite	0	infinite
RF-F	7-13	10.4	infinite	0	infinite
RF-W	7-15	23.7	infinite	0	infinite
Cutout	4-2	42.4	infinite	1.3E-07	151541
	4-7	33.6	infinite	0	infinite
	7-2	54.0	infinite	7.5E-07	25548
	7-4	42.5	infinite	3.5E-08	552578

7. Conclusions and remarks

In this paper, a bridge deck system using OSDs composited with SFRC layer is presented and applied to a real medium-span highway bridge. In order to demonstrate its structural feasibility. The stress and fatigue performance of OSDs were extensively investigated through field measurement under random traffic flows, combined with FEA model loaded by the AASHTO fatigue truck. The following conclusions and remarks can be reached.

1) Under random traffic flows, the stress levels at all OSDs details are relatively low, with the maximum stress ranges significantly lower than the CAFL of the corresponding details. Based on the maximum stress ranges and damage calculations, the fatigue life of the OSDs details far exceeds the 100-year design life of the bridge and hence the OSDs composited with SFRC system is a fatigue-resistant structure which can provide the OSDs with sufficient resistance against traffic loading.
2) Under wheel loading, the RD-R is identified as the more critical detail among the RD details, while RF-W experiences relatively larger stress among the RF details, and the cutout detail exhibits the highest stress level overall. These stress characteristics are consistently observed in both the FEA and the field measurements.
3) The OSDs composited with SFRC system significantly increases the stiffness of the OSDs and greatly reduce the local structural effects under wheel loads, resulting in significantly low stresses and displacement of the OSDs.
4) The stress from FEA modelling using the AASHTO fatigue truck are lower than the field measured results, suggesting that the HS-15 fatigue truck may represent a lower fatigue loading effect compared to the real average fatigue loading effect produced by the random traffic flows passing the bridge.

For small and medium-span bridges, since the dead loads are not the major concerns, based on the present study, the suggested deck system using the OSDs composited with SFRC layer is a fatigue-resistant structure and is a sound solution for small and medium-span highway bridges using the OSDs.

CRediT authorship contribution statement

Rui-Xu Zhu: Conceptualization, Data curation, Investigation, Methodology, Writing – original draft, Writing – review & editing. **Zhi-Wen Zhu:** Conceptualization, Data curation, Investigation, Methodology, Writing – review & editing. **Giuseppe Lacidogna:** Conceptualization, Data curation, Methodology, Visualization.

Declaration of competing interest

The authors declare that they have no known competing financial interests or personal relationships that could have appeared to influence the work reported in this paper.

Acknowledgment

Financial support for this study was provided by the National Natural Science Foundation of China under grant 52278509, and by the National Natural Science Foundation of Guangdong Province under grant 2022A1515010261, which the authors gratefully appreciate.

Data availability

Data will be made available on request.

References

AASHTO, 2017. AASHTO LRFD Bridge Design Specifications, eighth ed. American Association of State Highway and Transportation Officials, Washington, D.C., USA.

Blasi, G., Leone, M., 2022. Inverse analysis-based model for the tensile behaviour of fibre reinforced concrete with manufactured and waste tyres recovered fibres. Case Stud. Constr. Mater. 17, e01297. https://doi.org/10.1016/j.cscm.2022.e01297.

Bocci, E., Graziani, A., Canestrari, F., 2015. Mechanical 3D characterization of epoxy asphalt concrete for pavement layers of orthotropic steel decks. Constr. Build. Mater. 79, 145–152. https://doi.org/10.1016/j.conbuildmat.2014.12.120.

Caggiano, A., Xargay, H., Folino, P., Martinelli, E., 2015. Experimental and numerical characterization of the bond behavior of steel fibers recovered from waste tires embedded in cementitious matrices. Cem. Concr. Compos. 62, 146–155. https://doi.org/10.1016/j.cemconcomp.2015.04.015.

Chen, Z.Y., Li, C.X., Ke, L., Guo, L.C., Song, G.B., 2021. Fatigue crack repair and optimization of cope holes in orthotropic steel decks. China J. Highw. Transp. 34 (7), 96–107. https://doi.org/10.19721/j.cnki.1001-7372.2021.07.025.

Connor, R., Fisher, J., Gatti, W., Gopalaratnam, V., Kozy, B., Leshko, B., McQuaid, D.L., Medlock, R., Mertz, D., Murphy, T., Paterson, D., Sorensen, O., Yadlosky, J., 2012. Manual for Design, Construction, and Maintenance of Orthotropic Steel Deck Bridges. FHWA, Washington.

Cui, C., Zhang, Q., Hao, H., Li, J., Bu, Y., 2018. Influence of asphalt pavement conditions on fatigue damage of orthotropic steel decks: parametric analysis. J. Bridge Eng. 23 (12), 04018093. https://doi.org/10.1061/(ASCE)BE.1943-5592.0001313.

Ding, N., Shao, X.D., 2015. Study on fatigue performance of light-weighted composite bridge deck, China civ. Eng. J. 48 (1), 74–81. https://doi.org/10.15951/j.tmgcxb.2015.01.009.

EN 1993-1-9:2005, 2005. Eurocode 3: Design of Steel Structures - Part 1-9: Fatigue. European Committee for Standardization, Brussels, Belgium.

Fang, L., Fu, Z.Q., Ji, B.H., Fan, J., 2023. Reinforcement effect of high-strength bolts for stop-hole under out-of-plane bending loads. J. Bridge Eng. 28 (1), 04022129. https://doi.org/10.1061/JBENF2.BEENG-5711.

Fu, Z.Q., Ji, B.H., Zhang, C.Y., Wang, Q.D., 2017. Fatigue performance of roof and U-rib weld of orthotropic steel bridge deck with different penetration rates. J. Bridge Eng. 22 (6), 04017016. https://doi.org/10.1061/(ASCE)BE.1943-5592.0001036.

Fu, Z.Q., Wang, Y.X., Ji, B.H., Jiang, F., 2019. Effects of multiaxial fatigue on typical details of orthotropic steel bridge deck. Thin-Walled Struct. 135, 137–146. https://doi.org/10.1016/j.tws.2018.10.035.

Gao, Y.Q., Fu, Z.Q., Ji, B.H., Ji, B.C., 2025. The influence mechanism of structural characteristics on the fatigue cracking mode at the rib-to-deck welded joint. Eng. Struct. 345, 121376. https://doi.org/10.1016/j.engstruct.2025.121376.

GB/T 50081-2019, 2019. Standard for Test Methods of Concrete Physical and Mechanical Properties. The Ministry of Housing and Urban-Rural Development of the People's Republic of China, Beijing, China.

JG/T 472-2015. Steel Fiber Reinforced Concrete.

JTG D64-2015, 2015. Specification for design of highway steel Bridge. Ministry of Transportation of PRC. Beijing, China.

Krstulovic-Opara, N., Haghayeghi, A.R., Haidar, M., Krauss, P.D., 1995. Use of conventional and high-performance steel fiber reinforced concrete for bridge deck overlays. ACI Mater. J. 92 (6), 669–677. https://doi.org/10.14359/9787.

Li, C.X., Ke, L., Chen, Z.Y., He, J., Guo, L.C., Jiao, Y., 2021. Fatigue behavior and CFRP reinforcement of floorbeam cutouts in orthotropic steel bridge decks. China J. Highw. Transp. 34 (5), 63–75. https://doi.org/10.19721/j.cnki.1001-7372.2021.05.007.

Li, X.C., Fu, Z.Q., Shu, J.K., Ji, B.H., Ji, B.C., 2024. A modified physics-informed neural network to fatigue life prediction of deck-rib double-side welded joints. Int. J. Fatig. 189, 108566. https://doi.org/10.1016/j.ijfatigue.2024.108566.

Lim, H., Hashimoto, K., Sugiura, K., 2014. Influence of asphalt surfacing on fatigue evaluation of rib-to-deck joints in orthotropic steel bridge decks. J. Bridge Eng. 19 (10), 04014039. https://doi.org/10.1061/(ASCE)BE.1943-5592.0000610.

Martinelli, E., Caggiano, A., Xargay, H., 2015. An experimental study on the post cracking behaviour of hybrid industrial/recycled steel fibre-reinforced concrete. Constr. Build. Mater. 94, 290–298. https://doi.org/10.1016/j.conbuildmat.2015.07.007.

Meng, G.W., Wu, B., Xu, S.X., Huang, J.S., 2021. Modeling and experimental validation of flexural tensile properties of steel fiber reinforced concrete. Constr. Build. Mater. 273, 121974. https://doi.org/10.1016/j.conbuildmat.2020.121974.

Meng, T.S., Foster, S.J., Hitet, M.L., Htut, T.N.S., 2014. Mixed mode fracture behaviour of steel fibre reinforced concrete. Mater. Struct. 47, 67–76. https://doi.org/10.1617/s11527-013-0045-1.

Pei, B.D., Li, L.F., Shao, X.D., et al., 2019. Research on field measurement of steel-UHPC lightweight composite deck. J. Hunan Univ. (Nat. Sci.) 46 (1), 76–84. https://doi.org/10.16339/j.cnki.hdxbzkb.2019.01.008.

Picazo, A., Alberti, M.G., Galvez, J.C., 2021. Shear slip post-cracking behaviour of polyolefin and steel fibre reinforced concrete. Constr. Build. Mater. 290, 123187. https://doi.org/10.1016/j.conbuildmat.2021.123187.

Qin, S.Q., Zhang, J.B., Huang, C.L., et al., 2022. Fatigue performance evaluation of steel-UHPC composite orthotropic deck in a long-span cable stayed bridge under in-service traffic. Eng. Struct. 254, 113875. https://doi.org/10.1016/j.engstruct.2022.113875.

Shao, X.D., Cao, J.H., 2018. Fatigue assessment of steel-UHPC lightweight composite deck based on multi-scale FE analysis: case study. J. Bridge Eng. 23 (1), 05017015. https://doi.org/10.1061/(ASCE)BE.1943-5592.0001146.

Su, K., Yang, Y.Y., Cheng, B., He, C.X., Xu, Y., 2021. Study on the key points of UHPC construction of steel-mixed combination beam bridge paving. Urban Roads Bridges Flood Control (4), 167–169+21. https://doi.org/10.16799/j.cnki.csdqyfh.2021.04.045.

Tong, L.W., Shen, Z.Y., Chen, Z.Y., 1997. Fatigue load spectrum of urban roads and bridges, China Civ. Eng. J. 30 (5), 20–27. https://doi.org/10.15951/j.tmgcxb.1997.05.003.

Wang, C.S., Zhai, M.S., Houankpo, O.N., 2020. Fatigue strength of typical details in orthotropic steel bridge deck. Eng. Mech. 37 (8), 102–111. https://doi.org/10.6052/j.issn.1000-4750.2019.09.0518.

Wang, Q.D., Ji, B.H., Xia, J.Y., Fu, Z.Q., 2020. Fatigue assessment of rib-deck welds in orthotropic steel decks integrating the effect of load dispersal through asphalt surfacing. Structures 28, 1701–1712. https://doi.org/10.1016/j.istruc.2020.10.017.

Wu, C., Liu, H.Y., Zhang, Z.H., Sun, Y.M., 2013. Influence of pavements temperature on fatigue life of orthotropic deck of steel bridge. J. Tongji Univ. (Nat. Sci.) 41 (8), 1213–1218. https://link.cnki.net/urlid/31.1267.N.20130814.1759.011.

Xiang, Z., Zhu, Z.W., 2021. Fatigue behavior of closed rib-to-floor beam joint in steel-UHPC composite bridge decks. J. Railw. Sci. Eng. 18 (7), 1798–1807. https://doi.org/10.19713/j.cnki.43-1423/u.t20210184.

Xiao, Z.G., Yamada, K., Ya, S., Zhao, X.L., 2008. Stress analyses and fatigue evaluation of rib-to-deck joints in steel orthotropic decks. Int. J. Fatig. 30, 1387–1397. https://doi.org/10.1016/j.ijfatigue.2007.10.008.

Yang, R.N., 2012. Research on Static Damage and Fatigue Damage of Steel Fiber Reinforced Concrete, Ph.D. Dissertation. South China University of Technology, Guangzhou, China.

Ye, H.W., Yang, Z., Han, B., Duan, Z.C., Zhou, Y., 2021. Failure mechanisms governing fatigue strength of steel-SFRC composite bridge deck with U-ribs. J. Bridge Eng. 26 (4), 04021014. https://doi.org/10.1061/(ASCE)BE.1943-5592.0001692.

Yin, W.S., Su, E., Mansur, M., Hsu, T.C., 1988. Biaxial tests of plain and fiber concrete. ACI Mater. J. 86 (3), 236–243. https://doi.org/10.14359/2427.

Zhang, L.W., Zhao, H., Tan, C.J., Shao, X.D., Cao, J.H., 2016. Stress analysis on cutout at welded rib-to-floorbeam connections in a light-weight steel-UHPC composite deck. China J. Highw. Transp. 29 (9), 75–81. https://doi.org/10.19721/j.cnki.1001-7372.2016.09.009.

Zhang, Q.H., Bu, Y.Z., Li, Q., 2017. Review on fatigue problems of orthotropic steel bridge deck. China J. Highw. Transp. 30 (3), 14–30. https://doi.org/10.19721/j.cnki.1001-7372.2017.03.002.

Zhang, Q.H., Jin, T., Li, J., Bu, Y.Z., 2020. Study on reinforcement for fatigue cracking of rib-to-floorbeam welded joints of steel bridge deck. J. Southwest Jiao Tong Univ. 55 (1), 92–99. https://link.cnki.net/urlid/51.1277.u.20180522.2327.026.

Zhang, S.L., Zhang, C.S., Liao, L., Zhou, X.D., Li, W., 2020. Investigation into the effect of fibre distribution on the post-cracking tensile strength of SFRC through physical experimentation and numerical simulation. Constr. Build. Mater. 248, 118433. https://doi.org/10.1016/j.conbuildmat.2020.118433.

Zhao, Y., Wang, H., Li, L., Yi, H.Y., 2022. Overview of fatigue crack cause analysis and fatigue performance improvement measures for orthotropic steel bridge deck. Technol. Highw. Transp. (12), 37–42. https://doi.org/10.13607/j.cnki.gljt.2022.06.007.

Zhu, Z.W., Huang, Y., Wang, T., Wen, P.X., Xiang, J.J., 2016. Fatigue evaluation of composite bridge deck of Fochen expansion bridge under random traffic flows. Steel Constr. (Chin. Engl.) 31 (11), 31–37. https://doi.org/10.13206/j.gjg201611007.

Zhu, Z.W., Huang, Y., Wen, P.X., Chen, W., Yu, P., Shi, Y.G., et al., 2017a. Investigation on fatigue performance of orthotropic bridge deck with steel-UHPC composite system under random traffic flows. China J. Highw. Transp. 30 (3), 200–209, 0.19721/j.cnki.1001-7372.2017.03.022.

Zhu, Z.W., Huang, Y., Xiang, Z., Mai, P., 2017b. Fatigue performance of floorbeam cutout detail of orthotropic steel bridge on heavy freight transportation highway. China J. Highw. Transp. 30 (3), 104–112. https://doi.org/10.19721/j.cnki.1001-7372.2017.03.011.

Zhu, Z.W., Li, J.P., Tang, Q., 2023. Stress behaviors and mechanism of details of orthotropic steel deck under wheel loads. Eng. Mech. 40 (3), 163–174. https://doi.org/10.6052/j.issn.1000-4750.2021.09.0722.

Zhu, Z.W., Li, J.P., Zhong, G.C., Chen, X.W., Wang, L., 2022. Stress behavior of both side welded rib-to-deck details based on field tests and finite element analysis. China J. Highw. Transp. 35 (6), 36–48. https://doi.org/10.19721/j.cnki.1001-7372.2022.06.003.

Zhu, Z.W., Xiang, Z., Li, J.P., 2018b. Fatigue performance of floorbeam cutout on orthotropic steel bridge decks. J. Traffic Transp. Eng. 18 (2), 11–22. https://doi.org/10.19818/j.cnki.1671-1637.2018.02.002.

Zhu, Z.W., Xiang, Z., Zhou, Y.E., 2019. Fatigue behavior of orthotropic steel bridge stiffened with ultra-high performance concrete layer. J. Constr. Steel Res. 157, 132–142. https://doi.org/10.1016/j.jcsr.2019.02.025.

Zhu, Z.W., Yuan, T., Xiang, Z., Huang, Y., Zhou, Y.E., Shao, X., 2018a. Behavior and fatigue performance of details in an orthotropic steel bridge with UHPC-deck plate composite system under in-service traffic flows. J. Bridge Eng. (3), 04017142. https://doi.org/10.1061/(ASCE)BE.1943-5592.0001167.